Applied Catalysis B: Environmental 168-169 (2015) 465–471

Contents lists available at ScienceDirect

Applied Catalysis B: Environmental

journal homepage: www.elsevier.com/locate/apcatb

Fabrication of sulfur-doped g-C_3N_4/Au/CdS Z-scheme photocatalyst to improve the photocatalytic performance under visible light

Weibing Li*, Chang Feng, Shiyuan Dai, Jiguang Yue, Fangxia Hua, Hao Hou

School of Environment and Safety Engineering, Qingdao University of Science and Technology, 53# Zhengzhou Road, Qingdao 266042, China

ARTICLE INFO

Article history:
Received 31 October 2014
Received in revised form 9 January 2015
Accepted 12 January 2015
Available online 13 January 2015

Keywords:
Z-scheme photocatalyst
Sulfur doping g-C_3N_4
Gold nanoparticle
Sandwich nanostructure
Hydrogen evolution

ABSTRACT

Au and CdS nanoparticles were firstly deposited on the surface of g-CNS by two-step self-assembly process to afford sandwich-structured Z-scheme g-CNS/Au/CdS photocatalyst. The photocatalytic reduction of water to hydrogen was highly improved in lactic acid scavenger solution using the as-prepared g-CNS/Au/CdS than using g-CNS/CdS in the presence of visible light, and the photocatalytic degradation of RhB dye was also improved. According to the photoluminescence spectra and excited state electron radioactive decay lifetime, when Au was paired between g-CNS and CdS, based on the Z-scheme charge-carrier transfer mechanism, the redox ability of the photogenerated holes and electrons was enhanced, followed by the increased lifetime of the photoelectrons. Therefore, the photocatalytic ability of the g-CNS/Au/CdS composite was significantly improved.

1. Introduction

Since Fujishima and Honda found that water can be split into hydrogen by using TiO_2 as photoanode in 1972 [1], semiconductor photocatalysis was believed to be a promising route to address the environmental pollution and energy depletion problems and attracted wide attention of researchers [2–6]. However, TiO_2 can absorb the ultraviolet part (under 380 nm) of the solar spectrum because of its large bandgap (3.2 eV). Furthermore, a large amount of densities of trap states were formed in the surface and bulk of TiO_2 during the synthesis process, which could induce a fast electron–hole recombination during the light illumination [7]. To overcome the drawbacks of wide bandgap TiO_2, the semiconductors with narrow bandgap have been developed to efficiently utilize the visib1light in sunlight. Kudo et al. [8] prepared monoclinic $BiVO_4$ photocatalyst in aqueous media at room temperature, their further research found that this material has a high performance for O_2 evolution under visible light illumination. Yi et al. [9] reported an orthophosphate semiconductor Ag_3PO_4 which could absorbed visible light to decompose organic contaminants as well as oxidize water. Wang et al. [10] prepared Ag@AgCl by ion-exchange reaction and photo-assistance reduce method, and found that Ag@AgCl could decompose organic contaminants under visible light illumination by the plasmonic effect. However, the photocatalysis performance of those single materials could be limited by their drawbacks of low photo to electrons quantum yield and sharply photo-induced corrosion. In order to solve above problems, fabricating a heterojunction between two materials is a promising way to increase the separation efficiency of photo-induced electrons and holes as well as enhance the stability of those materials [11,12]. However, the redox ability of the photo-induced electrons and holes would be decreased as the heterojunction formation, so some novel heterojunction system should be developed to solve this contradiction.

Recently, Tada et al. [13] proposed the concept of all-solid-state Z-scheme photocatalysts in a sandwich-structured CdS/Au/TiO_2 photocatalyst, where Au nanoparticles (NPs) were anchored between CdS and TiO_2 and acted as electron transfer mediator. It was found that the photogenerated electrons in conduction band (CB) of TiO_2 could transfer through the Au layer and recombine with the photogenerated holes left in valance band (VB) of CdS. As a result, the photogenerated electrons and holes are left in the CB of CdS and the VB of TiO_2, respectively. Compared with the conventional *p–n* heterojunction-type photocatalysts, the Z-scheme photocatalytic system can remain the strong reducibility and oxidizability of the both photocatalysts [14–17]. To enhance the photocatalysis activity by using Z-scheme photocatalysts, we should make some further designs following the three points: (i) the two semiconductors used in Z-scheme system should have visible light response ability simultaneously, which enables them to capture more photons; (ii) the semiconductors in this system should have high redox stability in photocatalysis reaction solution;

* Corresponding author. Tel.: +86 0532 8402 2617; fax: +86 0532 8402 2617.
E-mail address: lwbing@qust.edu.cn (W. Li).

http://dx.doi.org/10.1016/j.apcatb.2015.01.012
0926-3373/

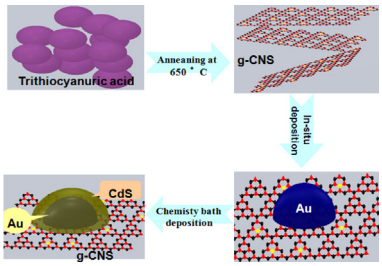

Scheme 1. Schematic illustration of the relevant preparation process of the g-CNS/Au/CdS Z-scheme photocatalyst.

and (iii) the electron transfer mediator layer anchored between the two semiconductors should tightly attached with both semiconductors.

Some previous works found that a well definite heterojunction can be formed between CdS and g-C_3N_4 compound because of the suitable band structure of the two semiconductors [18–20]. However, the system of g-C_3N_4/Au/CdS with two visible light responsive semiconductors, has not been reported so far. In this article, S-doped g-C_3N_4 (g-CNS) (After S-doping, the g-CNS could show more preferable visible light absorption ability and photocatalysis property) [21,22], a visible light responsive and high anti-reduction polymer semiconductor [23], was used to substitute wide band gap semiconductor material. Subsequently, to obtain a g-CNS/Au/CdS Z-scheme photocatalyst, we deposited Au NPs on the surface of the g-CNS, and attached CdS NPs on the surface of the Au NPs by bath deposition method. This typical z-scheme structure was characterized by using SEM, HRTEM, UV–vis diffuse refection spectrum, Photoluminescence spectra, excited state electron radioactive decay methodes. And as expected, this photocatalyst has a strongly photocatalysis water reduction to hydrogen evolution property under visible light illumination, since the photogenerated weak-reducing electrons from g-CNS transferred to the VB of CdS NPs through the Au NPs layer and recombined with the photogenerated weak-oxidizing holes from CdS.

2. Experimental methods

2.1. Photocatalyst preparation

Three grams trithiocyanuric acid was sintered at 650 °C with a heating rate of 10 °C min^{-1} under Ar atmosphere for 2 h to prepare g-CNS [23]. 0.2 g g-CNS was sonicated in 50 mL deionized water for 10 min and then 5 wt% chloroauric acid (10 mg L^{-1}) was added with stirring. NaOH solution was added until the pH value was 4.5 and then kept stirring for 4 h. The product was centrifuged and rinsed with water, dried at 60 °C for 24 h to obtain g-CNS/Au. At last, CdS was deposited on g-CNS/Au by bath deposition method. The prepared g-CNS/Au was dispersed into a clear solution of 10 mmol $Cd(NO_3)_2$ and 10 mmol CH_3CSNH_2, followed by water bath under stirring at 60 °C for 30 min. The product was then centrifuged, rinsed with water and ethanol, dried at 60 °C overnight. The procedure is shown as Scheme 1. Pure CdS was also prepared by bath deposition method but without rinse and drying. All reagents used in this study were analytical grade ones from Aladin Industrial Corporation, China, without any further purification.

2.2. Characterization

The morphology of the prepared samples was analyzed using a scanning electron microscope (SEM, JSM-6700F; JEOL, Tokyo, Japan). X-ray diffraction (XRD, D/MAX-2500/PC; Rigaku Co., Tokyo, Japan) was used to identify the crystalline structures of the series samples. The morphology of the all-solid-state CdS/Au/g-CNS was observed using field emission transmission electron microscope (FE-HRTEM, Tecnai G2 F20, FEI Company, USA). The elementary composition and bonding information of the synthesized CdS/Au/g-CNS three phase material were analyzed using energy dispersive spectrometer (EDS, FEI Tecnai G20, FEI Company, USA) and X-ray photoelectron spectroscopy (XPS, Axis Ultra, Kratos Analytical Ltd., England). UV-visible diffuse reflectance spectrophotometer (U-41000; HITACHI, Tokyo, Japan) was used to study the optical absorption properties of the series samples. The photoluminescence intensity and excited state electron radioactive decay of the prepared photocatalysts were characterized using a fluorescence spectrometer (PL, Fluoro Max-4, HORIBA Jobin Yvon, France).

2.3. Photocatalytic water splitting and dyes degradation testing

In the photocatalytic water splitting test, 0.1 g photocatalyst was used and the solution was a mixture of 20 mL lactic acid and 80 mL deionized water. Before the test, the photo-reaction system was vacuumed until the pressure gage was stable. Externally illuminating 300 W Xe lamp (PLS-SXE300, Beijing Changtuo Co., Ltd., China) was used as white light source and visible light was achieved using a 420 nm cut-off filter to remove ultraviolet light. The distance between the light source and the solution that produced hydrogen was 10 cm. The testing temperature was maintained at 5 °C by condensate water system. In the dyes degradation test, 0.1 g photocatalyst was used and dyes to be degraded was 100 mL Rhodamine B (RhB) solution, methyl orange (MO) solution, and methylene blue (MB) solution, the concentration of which were all 10 mg/L. Before the degradation test, the dyes were mixed with photocatalyst and kept stirring for 30 min in dark to reach adsorption equilibrium. Externally illuminating 300 W Xe lamp (PLS-SXE300, Beijing Changtuo Co., Ltd., China) was used as white light source and visible light was achieved using a 420 nm cut-off filter to remove ultraviolet light. The distance between light source and the dye solution was 10 cm. The testing temperature was maintained at 25 °C by condensate water system.

3. Results and discussion

The XRD patterns of the composites are shown in Fig. 1. Curve 1a shows the XRD curve of g-CNS. The diffraction peaks at 13.0° and 27.8° correspond to the (100) and (002) crystal planes [24], respectively. After the deposition of Au NPs, the characteristic diffraction of Au (JCPDS 80–0019) at 38.2° and 44.3° were detected from XRD pattern of g-CNS/Au (see curve 1b). The subsequent attachment of CdS NPs on the Au NPs layer resulted in the

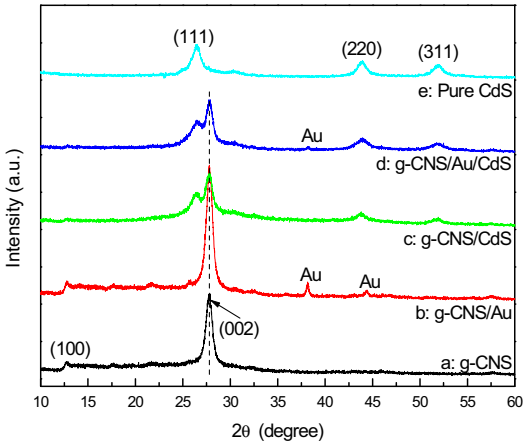

Fig. 1. XRD patterns of different samples (a) g-CNS; (b) g-CNS/Au; (c) g-CNS/CdS; (d) g-CNS/Au/CdS; and (e) pure CdS.

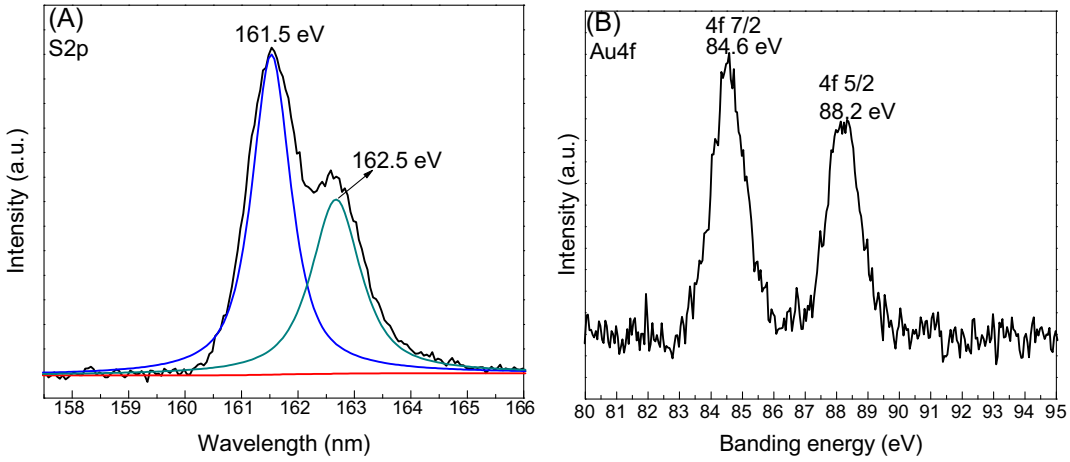

Fig. 2. XPS of the elements of g-CNS/Au/CdS composite material (A) Au 4f and (B) S 2p.

formation of the Z-scheme structure, and the typical diffraction peaks of (1 1 1), (2 2 0), and (3 1 1) crystal planes of cubic CdS were observed at 26.4°, 43.9°, and 51.9° (JCPDS 80–0019) from the diffraction pattern of the g-CNS/Au/CdS triple-phase composite (see curve 1d), respectively. Besides, pure cubic CdS NPs and g-CNS/CdS composite were prepared to compare their photocatalytic performance, and their XRD patterns are displayed in Fig. 1 (curves 1c and e).

Elementary composition and valence bond structure of the g-CNS/Au/CdS composite were characterized by X-ray photoelectron spectroscopy (XPS). Fig. 2a shows the S 2p peaks at 161.5 eV and 162.5 eV, which is ascribed to the S in CdS [18,19]. However, the S–N peak at 164.0 eV was not observed due to a low doping concentration of S in g-C_3N_4. Furthermore, the top Cd–S layer could block the signal of S–N, since XPS technique can only probe the elemental composition of the surface region (<10 nm thick) [25]. Fig. 2b shows the XPS spectrum of Au 4f with the characteristic peaks at 83.6 eV and 88.2 eV of Au^0, confirming the existence of Au^0 in the composite [15,26]. Fig. S1a shows the XPS survey spectrum of the g-CNS/Au/CdS composite, indicating the presence of C, N, Cd, S, and Au in the composite. Figure S1b shows the XPS spectrum of N at 398.8 eV, 399.9 eV, and 401.2 eV corresponding to C—N—C, C—$[N]_3$, and C—NH_x, respectively [27]. Fig. S1c shows the XPS spectrum for C, and the peaks at 288.1 eV and 284.6 eV correspond to C—N—C and C—C, respectively. The peak of C—O was not observed because of the high degree of reduction of g-CNS [27]. The photoelectron S2p peaks for the Cd element were observed at 405.6 eV and 412.3 eV (Fig. S1d), which can be assigned to the Cd^{2+} ions of the CdS.

Fig. 3A shows the SEM image of g-CNS, illustrating that g-CNS had a similar structure as graphite, with a clean and smooth surface. Fig. 2B shows the SEM morphology of g-CNS after the Au deposition. Some large Au nanoparticles were observed directly on the surface of g-CNS by SEM. Fig. 3A shows the SEM image of the g-CNS/Au/CdS. Clearly, numerous CdS NPs with diameter of 30–50 nm were observed on the surface of the flake structure of g-CNS. The elements mapping of g-CNS/Au/CdS results showed in Figure S2, the image indicated that the sample was formed by the elements of C, N, Cd, S and Au, at the same time, the Au and CdS loaded on the surface of g-CNS. Fig. 3D shows the TEM image of g-CNS/Au/CdS, highlighting a large area of the flake structure of the g-CNS with many dark particles. These particles were the Au nanoparticles deposited on the surface of g-CNS, and each Au nanoparticle was covered by brighter CdS layer. The black region in this figure was zoomed in as Fig. 3E, showing the granular or rod-like Au nanoparticles with a length of 20 nm and width of 40 nm, and the diameter of the surrounding CdS was ~80 nm. The inset shows the EDS spectrum of this sample. C, N, S, Cd, and Au were observed as the elements in the g-CNS/Au/CdS composite. The O might come from the adapted CO_2, whereas the Cu possibly originated from the Cu substrate in TEM image. Fig. 3F shows the high-resolution TEM morphology and the (1 1 1) crystal plane of the CdS nanoparticles. The phase contact of the g-CNS-Au-Cds composite was excellent. According to the results of XRD, XPS, SEM, and TEM microscopy analyses, the g-CNS/Au/CdS three phase composite was successfully prepared. Figure S3 shows the transmission electron microscopy (TEM) image of the g-CNS/CdS, and the flake g-CNS and brighter CdS nanoparticles deposited on the surface were observed.

The UV–vis absorption spectra of the composites are shown in Fig. 4. Curves 4a and b show the UV–vis absorption spectra of g-CNS and g-CNS/Au, respectively. The absorption intensity of g-CNS did not change significantly after the Au deposition. It only caused a small red shift in the absorption and a little decrease in UV absorption. Both the g-CNS and g-CNS/Au had strong absorption at wavelength shorter than 450 nm, originating from the excitation from P_z orbital of N atom to P_z empty orbital of C atom. The weak absorption at wavelength longer than 450 nm was due to the excitation of the P_z orbital of N atom to the doped S orbital. Curve 4e shows the UV–vis absorption of CdS, indicating that the pure CdS on the edge of the absorption peak was at ~560 nm with a strong absorption of photons with wavelength shorter than 560 nm. The UV–vis absorption spectra of g-CNS/CdS and g-CNS/Au/CdS are displayed in curves 4c and d, respectively. Obviously, the cut-offs of g-CNS/Au/CdS and g-CNS/CdS absorptions were at ~560 nm and 540 nm, respectively, in the visible region. However, in the UV region, the absorption of g-CNS/CdS was stronger than that of g-CNS/Au/CdS, due to the fact that surface plasma resonance effect mainly located in the visible region instead of the UV region, thereby the different absorption of g-CNS/CdS and g-CNS/Au/CdS in the UV–vis region. In contrast to Curve 4e, the absorption of g-CNS/CdS and g-CNS/Au/CdS was weaker than that of the pure CdS within the entire region because of the presence of g-CNS. Nevertheless, the light absorption of semiconductor does not fully reflect its photocatalytic ability, because the photocatalysis process includes photo-capture, photoelectron transition, and interface photocatalysis, etc. Therefore, the further evaluation of the photocatalytic performance of the composite is necessary.

To evaluate the photocatalytic performance of the composite, its photocatalytic ability to reduce water to hydrogen in the lactic acid solution was measured. Fig. 5A shows the curves of photocatalytic hydrogen production yields of g-CNS, g-CNS/Au, g-CNS/CdS, g-CNS/Au/Cds and prure CdS, indicating that the hydrogen production

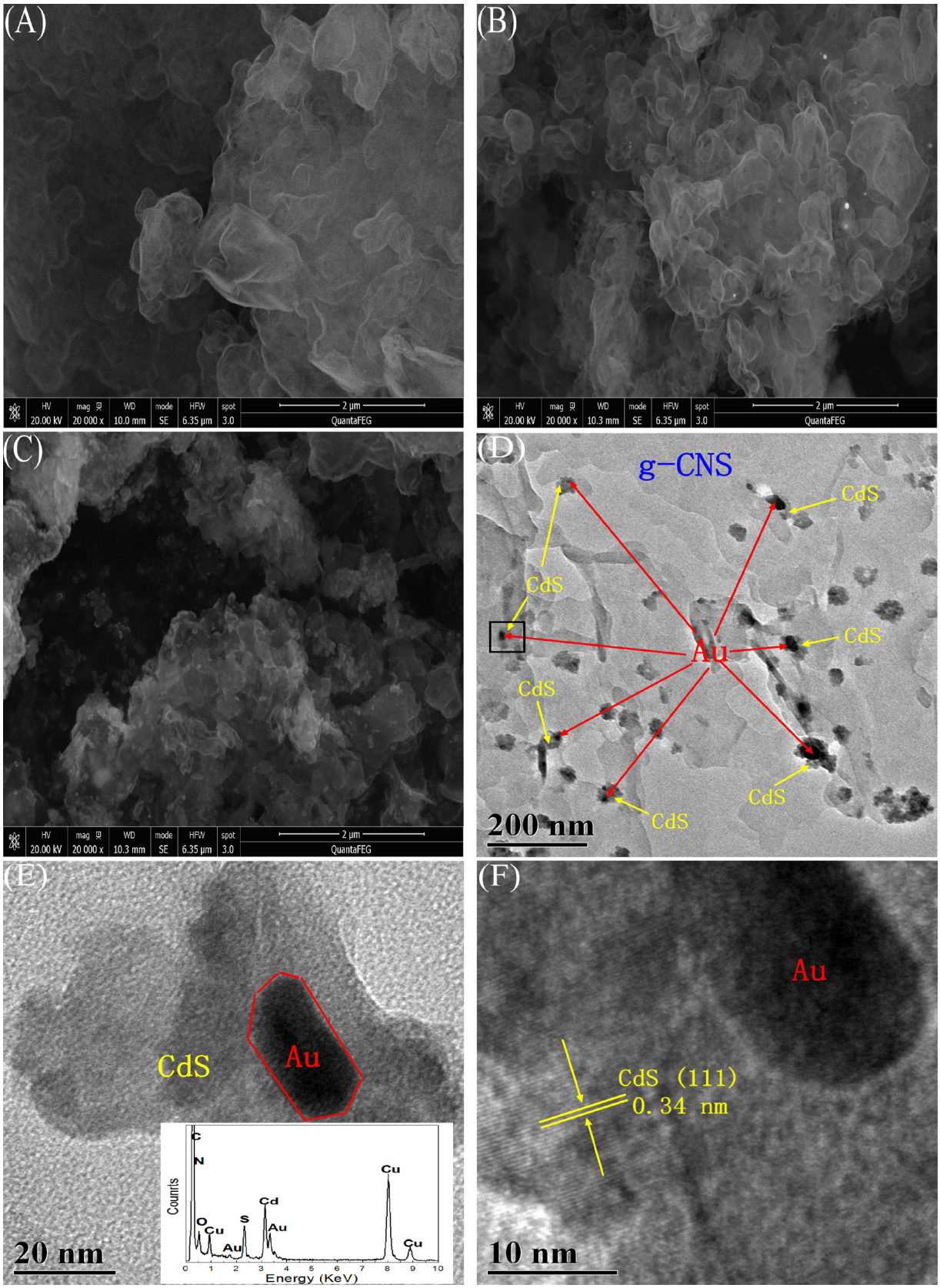

Fig. 3. SEM of (A) g-CNS; (B) g-CNS/Au; (C) g-CNS/Au/CdS; and TEM of g-CNS/Au/CdS (D) low resolution; (E) g-CNS/Au/CdS unit and its corresponding EDS result; and (F) high resolution.

from the pure g-CNS was very low and was only 15.4 μmol after light exposure for 5 h. After the deposition of 5 wt% Au, the catalytic performance of the g-CNS/Au was better than that of the pure CdS with 39.5 μmol of hydrogen production after exposure for 5 h, because of the auxiliary catalysis of Au. Fig. 5Ae shows that the pure CdS generated 126.6 μmol hydrogen after 5 h exposure because of the contribution of expanded visible-light absorption range. Fig. 5Ac shows that the hydrogen yield using g-CNS/CdS reached 322.7 μmol after 5 h exposure, and its catalytic ability was substantially improved compared to those of g-CNS, g-CNS/Au, and pure CdS. This was resulted by the heterojunction electric field between the CdS and g-CNS. This electric field could dramatically improve the efficiency of photoelectrons generation and holes separation, thus increase the photocatalytic hydrogen generation. Curve 5Ad shows the photocatalytic hydrogen generation curve using the g-CNS/Au/CdS Z-scheme photocatalyst, indicating that the hydrogen yield reached to 530 μmol after 5 h exposure, demonstrating even higher catalytic performance compared to that of g-CNS/CdS. This result indicates that when existing between the g-CNS and CdS, Au functioned as an electron transition system, enhancing the catalytic ability. Fig. 5B shows the photocatalytic stability measurement of g-CNS/Au/CdS. Every measurement cycle was for 5 h with new prepared vacuum system for each cycle. After five cycles, hydrogen production yield was 484.2 μmol with 8.7% decrease compared to 530 μmol in the first cycle, confirming that the g-CNS/Au/CdS photocatalyst was quite stable with the lactic acid scavenger.

Fig. 6 shows the measured dye degradation ability of the composites. Fig. 6A shows the degradation curves of RhB using the g-CNS, g-CNS/Au, g-CNS/CdS, g-CNS/Au/CdS, and pure CdS photocatalysts. Curve 6Aa shows the degradation of RhB using g-CNS. After 30 min dark adsorption equilibrium, ~33% of RhB was adsorbed, because of the enlarged g-CNS specific surface area caused by the generation of large amount of H_2S and NH_3 during its preparation. After 13 min exposure, RhB was completely degraded, indicating that g-CNS was able to easily degrade RhB. Curve 6A(b) shows the degradation of RhB using g-CNS/Au. Compared to g-CNS, owing to the deposition, Au might occupy some active spots on the surface, the adsorption and photocatalytic abilities were decreased. RhB was not fully degraded even after 15 min exposure. Curves 6A(c) and (e) shows the photocatalytic degradation of RhB using g-CNS/CdS and pure CdS, exhibiting similar performance of both completing degradation within 10 min, and their performances were improved than that of the pure g-CNS. Curve 6A(d) shows the RhB degradation using g-CNS/Au/CdS photocatalyst, indicating that a much improved performance of completing RhB degradation within 5 min. Fig. 6B shows the degradation performance curve

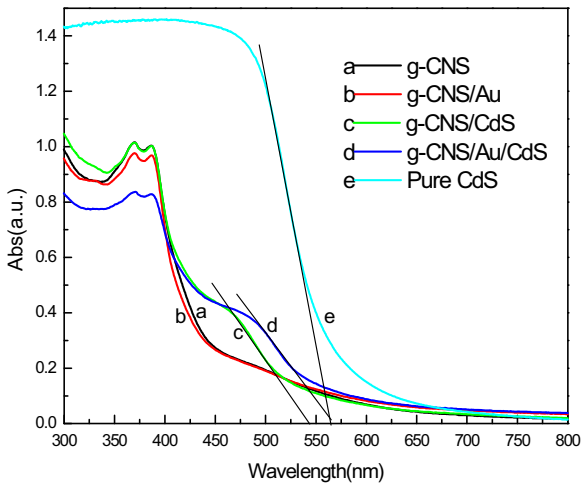

Fig. 4. UV–vis absorption spectra of (a) g-CNS; (b) g-CNS/Au; (c) g-CNS/CdS; (d) g-CNS/Au/CdS; and (e) pure CdS.

of RhB, MB, and MO using the g-CNS/Au/CdS Z-scheme. RhB and MB could be oxidized by photogenerated holes directly or by OH−, while MO could be oxidized and decomposed by $O_2^{\bullet}$ formed by the photoelectrons and O_2. Fig. 6B shows that RhB, MB, and MO were degraded completely by the g-CNS/Au/CdS Z-scheme photocatalyst in 10 min. Therefore, the results showed that both the holes and electrons generated by this photocatalyst had strong redox ability.

For most semiconductors, photogenerated electrons and holes can bind after the excitation by incident light, leading to the transfer of partial energy to fluorescence. Binding efficiency and photoelectron lifetime can be measured by monitoring fluorescence intensity and lifetime. Photoluminescence spectra and decay time of photoelectrons of the g-CNS/CdS and g-CNS/Au/CdS photocatalyts were measured to characterize the effect of Au in the g-CNS/Au/CdS photocatalyst (Fig. 7). Fig. 7A shows the photoluminescence spectra of g-CNS/CdS and g-CNS/Au/CdS, indicating a strong fluorescence peaks in the 400–750 nm range for both catalysts. Apparently, the fluorescence peak intensity of g-CNS/Au/CdS was much weaker than that of g-CNS/CdS, because Au inhibited the binding efficiency between photogenerated holes and electrons. Fig. 7B shows the excited state electron radioactive decay lifetime of g-CNS/CdS and g-CNS/Au/CdS. The photoelectron lifetimes of g-CNS and g-CNS/Au/CdS were 28.1 ns and 55.6 ns, respectively, indicating

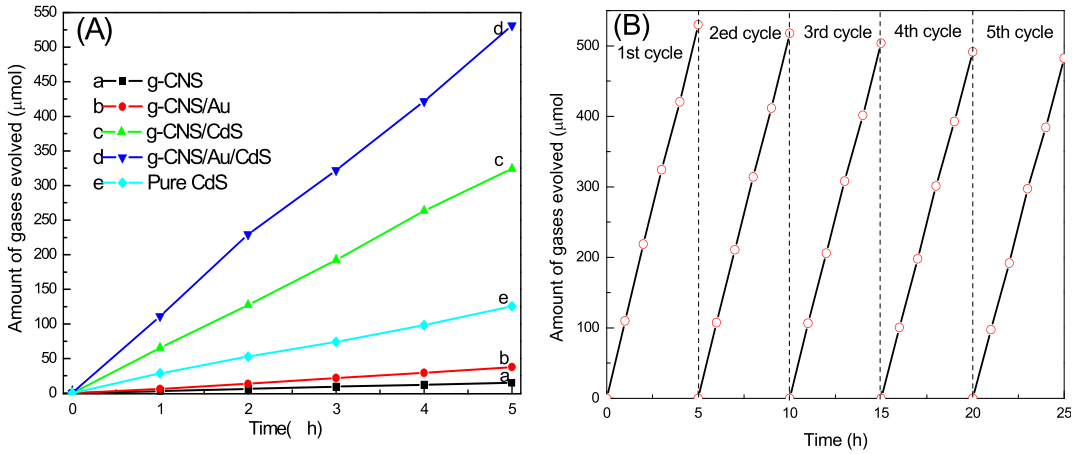

Fig. 5. (A) photocatalysis Hydrogen evolution ability of g-CNS, g-CNS/Au, g-CNS/CdS, g-CNS/Au/CdS and pure CdS in an aqueous solution containing lactic acid and (B) g-CNS/Au/CdS evacuated per 5 h without renewing the sacrificial agents.

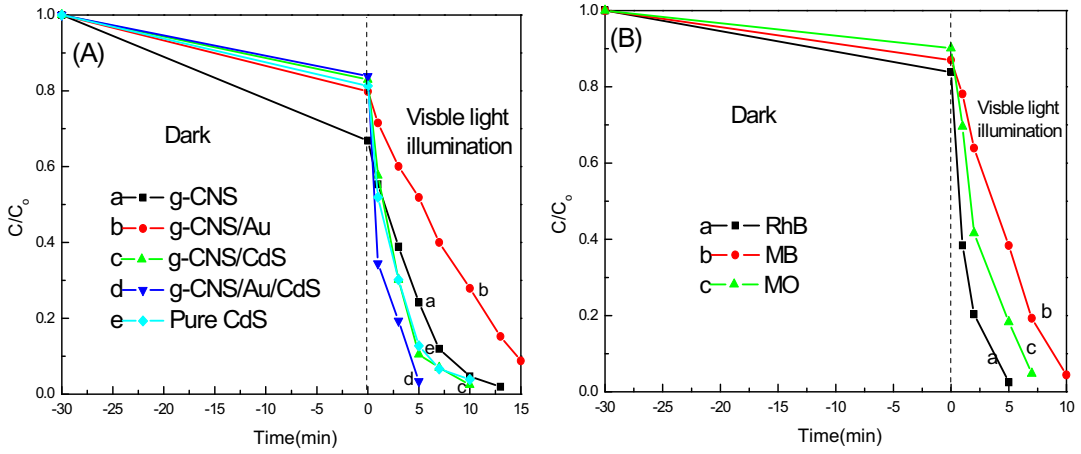

Fig. 6. (A) Photocatalysis degradation RhB performance of g-CNS, g-CNS/Au, g-CNS/CdS, g-CNS/Au/CdS, and pure CdS. (B) Photocatalysis degradation of RhB, MB, and MO dyes by g-CNS/Au/CdS photocatalyst.

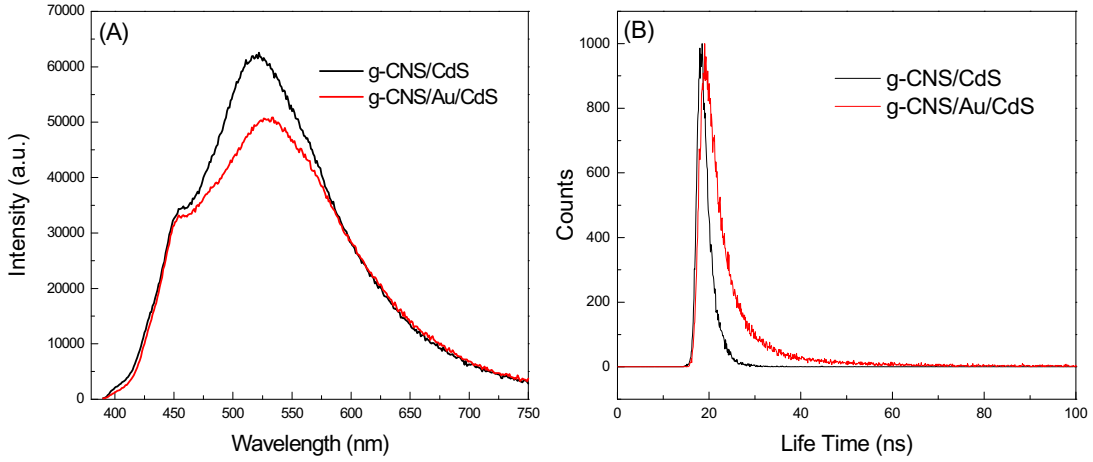

Fig. 7. (A) Photoluminescence spectra of g-CNS/CdS and g-CNS/Au/CdS and (B) excited state electron radioactive decay of g-CNS/CdS and g-CNS/Au/CdS.

that the incorporation of Au increased the photoelectron lifetime of the g-CNS/Au/CdS photocatalyst.

Fig. 8 is the proposed mechanism for Z-scheme charge-carrier transfer process in the g-CNS/Au/CdS photocatalyst. The in situ deposited Au paired between the g-CNS and CdS can participate in the transition process of photogenerated charge carrier. The weak reductive photoelectrons excited from CdS could be transferred to Au very fast. Moreover, the weak holes excited from g-CNS could also be quickly transferred to Au. Then photogenerated electrons and holes could annihilate at Au. In the meantime, the strong reductive photoelectrons would be left on the conduction band of CdS, and the strong oxidizing holes would be left on the valence band of g-CNS. These photogenerated electrons can be involved in the H^+ to H_2 reduction process and the holes might be involved in the oxidation reaction of lactic acid. According to the Z-scheme charge-carrier transfer process, the oxidation/reduction ability of photogenerated holes and electrons could be enhanced, and the lifetime of photocavities from CdS and photoelectrons from g-CNS could be increased, thus enhancing the catalytic ability.

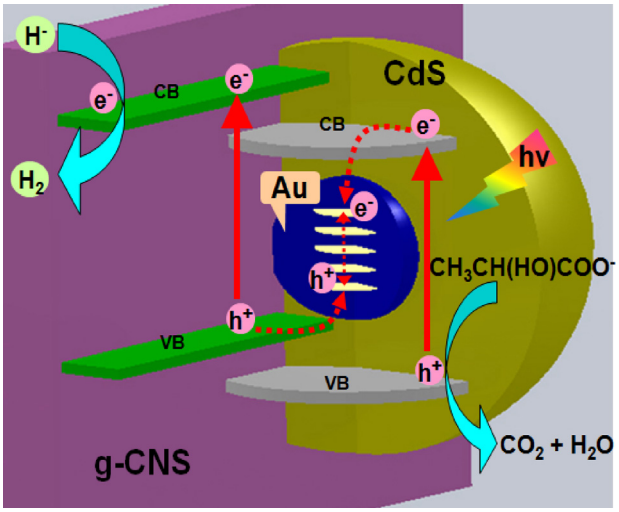

Fig. 8. Proposed mechanism for Z-scheme charge-carrier transfer process in the g-CNS/Au/CdS photocatalyst.

4. Conclusion

In this study, the g-CNS/Au/CdS Z-scheme photocatalyst was prepared in two steps: (1) Au nanoparticle was in situ deposited on the surface of g-CNS and (2) CdS nanoparticles were deposited on the surface of Au by chemical bath deposition reaction. The elementary analysis, crystal structure, and microstructure analysis revealed that Au successfully paired between g-CNS and CdS as an intermediate agent for efficient photoelectron transition. The g-CNS/Au/CdS photocatalyst exhibited better catalytic ability for

visible light hydrogen production and dye degradation than those of the g-CNS, g-CNS/Au, g-CNS/CdS, and pure CdS. The photoluminescence spectra and excited state electron radioactive decay lifetime showed that the photocatalytic ability of the composite was enhanced by increasing lifetime of photogenerated holes and electrons and boosting its redox ability through the Z-scheme charge-carrier transfer mechanism of the g-CNS/Au/CdS photocatalyst.

Acknowledgements

This work was financially supported by the Natural Science Foundation of China (41376126) and Foundation of Key Laboratory of Marine Environmental Corrosion and Bio-fouling, Institute of Oceanology, Chinese Academy of Sciences.

Appendix A. Supplementary data

Supplementary data associated with this article can be found, in the online version, at http://dx.doi.org/10.1016/j.apcatb.2015.01.012.

References

[1] A. Fujishima, K. Honda, Nature 238 (1972) 37–38.
[2] K. Maeda, J. Photochem. Photobiol. C: Photochem. Rev. 12 (2011) 237–268.
[3] G. Liu, J.C. Yu, G.Q. Lu, H.M. Cheng, Chem. Commun. 47 (2011) 6763–6783.
[4] N. Serpone, A.V. Emeline, J. Phys. Chem. Lett. 3 (2012) 673–677.
[5] H. Kisch, Angew. Chem. Int. Ed. 52 (2013) 812–847.
[6] Y.Y. Bu, Z.Y. Chen, J. Power Sources 272 (2014) 647–653.
[7] X.B. Chen, S.H. Shen, L.J. Guo, S.S. Mao, Chem. Rev. 110 (2010) 6503–6570.
[8] A. Kudo, K. Omori, H. Kato, J. Am. Chem. Soc. 121 (1999) 11459–11467.
[9] Z. Yi, J. Ye, N. Kikugawa, T. Kako, S. Ouyang, H.S. Williams, H. Yang, J. Cao, W. Luo, Z. Li, Y. Liu, R.L. Withers, Nat. Mater. 9 (2010) 559–564.
[10] P. Wang, B. Huang, X. Qin, X. Zhang, Y. Dai, J. Wei, M.H. Whangbo, Angew. Chem. Int. Ed. 47 (2008) 7931–7933.
[11] A. Kudo, Y. Miseki, Chem. Soc. Rev. 38 (2009) 253–278.
[12] M. Wang, L. Sun, Z. Lin, J. Cai, K. Xie, C. Lin, Energy Environ. Sci. 6 (2013) 1211–1220.
[13] H. Tada, T. Mitsui, T. Kiyonaga, T. Akita, K. Tanaka, Nat. Mater. 5 (2006) 782–786.
[14] A.J. Bard, M.A. Fox, Acc. Chem. Res. 28 (1995) 141–145.
[15] J.T. Li, S.K. Cushing, P. Zheng, T. Senty, F. Meng, A.D. Bristow, A. Manivannan, N.Q. Wu, J. Am. Chem. Soc. 136 (2014) 8438–8449.
[16] X.W. Wang, G. Liu, L.Z. Wang, Z.G. Chen, G.Q. Lu, H.M. Cheng, Adv. Energy Mater. 2 (2012) 42–46.
[17] A. Iwase, Y.H. Ng, Y. Ishiguro, A. Kudo, R. Amal, J. Am. Chem. Soc. 133 (2011) 11054–11057.
[18] J.Y. Zhang, Y.H. Wang, J. Jin, J. Zhang, Z. Lin, F. Huang, J.G. Yu, ACS Appl. Mater. Interfaces 5 (2013) 10317–10324.
[19] L. Ge, F. Zuo, J.K. Liu, Q. Ma, C. Wang, D.Z. Sun, L. Bartels, P.Y. Feng, J. Phys. Chem. C 116 (2012) 13708–13714.
[20] S.W. Cao, Y.P. Yuan, J. Fang, M.M. Shahjamali, F.Y.C. Boey, J. Barber, S.C.J. Loo, C. Xue, Int. J. Hydrogen Energy 38 (2013) 1258–1266.
[21] G. Liu, P. Niu, C. Sun, S.C. Smith, Z. Chen, G.Q. Lu, H. Cheng, J. Am. Chem. Soc. 132 (2010) 11642–11648.
[22] J. Zhang, J. Sun, K. Maeda, K. Domen, P. Liu, M. Antonietti, X. Fua, X. Wang, Energy Environ. Sci. 4 (2011) 675–678.
[23] L. Zhang, D. Jing, X. She, H. Liu, D. Yang, Y. Lu, J. Li, Z. Zheng, L. Guo, J Mater. Chem. A 2 (2014) 2071–2078.
[24] X.C. Wang, K. Maeda, A. Thomas, K. Takanabe, G. Xin, J.M. Carlsson, K. Domen, M. Antonietti, Nat. Mater. 8 (2008) 76–80.
[25] Z. Zheng, J. Zhao, Y. Yuan, H. Liu, D. Yang, S. Sarina, H. Zhang, E.R. Waclawika, H. Zhu, Chem. Eur. J. 19 (2013) 5113–5119.
[26] Z.B. Yu, Y.P. Xie, G. Liu, Lu X.L. Ma, H. Cheng, J. Mater. Chem. A 1 (2013) 2773–2776.
[27] D.J. Martin, K. Qiu, S.A. Shevlin, A.D. Handoko, X. Chen, Z. Guo, J. Tang, Angew. Chem. Int. Ed. 53 (2014) 1–7.